UC San Diego
UC San Diego Previously Published Works

Authors

Kroeger, Heike
Grimsey, Neil
Paxman, Ryan
et al.

The unfolded protein response regulator ATF6 promotes mesodermal differentiation

Heike Kroeger[1], **Neil Grimsey**[2], **Ryan Paxman**[3], **Wei-Chieh Chiang**[1], **Lars Plate**[3,4], **Ying Jones**[5], **Peter X. Shaw**[6], **JoAnn Trejo**[2], **Stephen H. Tsang**[7], **Evan Powers**[3], **Jeffery W. Kelly**[3], **R. Luke Wiseman**[3], and **Jonathan H. Lin**[1,8,*]

[1]Department of Pathology, University of California, San Diego, La Jolla, CA 92093, USA

[2]Department of Pharmacology, University of California, San Diego, La Jolla, CA 92093, USA

[3]Department of Molecular Medicine, Scripps Research Institute, La Jolla, CA 92037, USA

[4]Departments of Chemistry and Biological Sciences, Vanderbilt University, Nashville, TN 37235, USA

[5]Department of Cellular and Molecular Medicine, University of California, San Diego, La Jolla, CA 92093, USA

[6]Department of Ophthalmology, University of California, San Diego, La Jolla, CA 92093, USA

[7]Jonas Children's Vision Care and Bernard & Shirlee Brown Glaucoma Laboratory, Departments of Ophthalmology, Pathology and Cell Biology, Edward S. Harkness Eye Institute, New York Presbyterian Hospital, Columbia University, New York, NY 10032, USA

[8]VA San Diego Healthcare System, San Diego, CA 92161, USA

Abstract

ATF6 encodes a transcription factor that is anchored in the endoplasmic reticulum (ER) and activated during the unfolded protein response (UPR) to protect cells from ER stress. Deletion of the isoform activating transcription factor 6α (ATF6α) and its paralog ATF6β results in embryonic lethality and notochord dysgenesis in nonhuman vertebrates, and loss-of-function mutations in ATF6α are associated with malformed neuroretina and congenital vision loss in humans. These phenotypes implicate an essential role for ATF6 during vertebrate development. We investigated this hypothesis using human stem cells undergoing differentiation into multipotent

germ layers, nascent tissues, and organs. We artificially activated ATF6 in stem cells with a small-molecule ATF6 agonist and, conversely, inhibited ATF6 using induced pluripotent stem cells from patients with *ATF6* mutations. We found that ATF6 suppressed pluripotency, enhanced differentiation, and unexpectedly directed mesodermal cell fate. Our findings reveal a role for ATF6 during differentiation and identify a new strategy to generate mesodermal tissues through the modulation of the ATF6 arm of the UPR.

INTRODUCTION

The endoplasmic reticulum (ER) is a membrane-bound organelle found in all eukaryotic cells that is essential for protein folding, lipid/sterol synthesis, and free calcium storage (1). Molecular pathologies, such as protein misfolding, can upset ER function, leading to ER stress (2). Unabated ER stress is damaging to cells, and eukaryotes have evolved a conserved regulatory mechanism, called the unfolded protein response (UPR), to prevent ER stress and maintain intracellular homeostasis (3). In mammalian cells, the UPR is regulated by three ER-resident transmembrane proteins—inositol-requiring enzyme 1 (IRE1), protein kinase R-like ER kinase (PERK), and activating transcription factor 6 (ATF6)—that initiate transcriptional and translational programs in response to ER stress (3). The UPR expands the biosynthetic capacity of the ER by up-regulating protein folding enzymes and chaperones. Concomitantly, UPR activation enhances degradation of irreparably damaged or misfolded proteins and slows protein translation. By these mechanisms, the UPR helps cells cope with and survive episodes of ER stress.

In human cells, ATF6 is a 670–amino acid type II transmembrane protein whose luminal domain is posttranslationally modified after synthesis in the ER by N-linked glycosylation and intra- and intermolecular disulfide bridge formation that generate monomeric and oligomeric ATF6, as well as heteromeric complexes with other ER proteins (4, 5). In response to ER stress, ATF6 is fully reduced to a monomer that is then competent to exit the ER and shuttle via coat protein complex II (COPII) vesicles to the Golgi apparatus where site 1 and site 2 proteases cleave ATF6 in the transmembrane domain to liberate ATF6(N), the N-terminal cytosolic domain of ATF6 (6–8). ATF6(N) is a basic leucine zipper (bZIP)–class transcriptional activator that, once untethered from the membrane, migrates to the nucleus to up-regulate ER protein–folding chaperones and enzymes, such as GRP78/BiP (9, 10). ATF6 activation thus plays a key role in expanding the functional capacity of the ER during the UPR.

Loss of ATF6 disrupts ER homeostasis, leading to increased ER stress–induced damage and cell death (11–13). In mammals, ATF6 dysfunction leads to pathology in numerous experimental disease models associated with ER stress including hepatic steatosis, obesity, heart ischemia, stroke, diabetes, and neurodegeneration (14–21).

In addition to maintaining cellular and tissue health throughout life, emerging studies suggest that ATF6 also plays an essential role in vertebrate embryogenesis and early development. In specialized cell lines, ATF6 can transcribe genes involved in muscle or cartilage development (22, 23). Transgenic fish in which ATF6 activity is detected by a green fluorescent protein (GFP) reporter reveal ubiquitous GFP expression during

embryogenesis with especially pronounced signals in developing neuroectodermal structures, liver, and gut (24). Genetic ablation of ATF6α and its close paralog, ATF6β, results in embryonic lethality in both fish and mice (13, 25). Failure of notochord organogenesis has been specifically identified as the key malformation in these embryonic fish (25).

In humans, loss-of-function mutations in ATF6α have recently been identified in patients with heritable photoreceptor diseases including achromatopsia and cone-rod dystrophy (11, 26–29). A common feature in these patients is congenital malformation of the fovea, a unique region of the primate neuroretina packed with cone photoreceptors but devoid of retinal vasculature (30, 31). Patients carrying mutant ATF6α alleles fail to develop this structure (foveal hypoplasia), have abrogated photoreceptor function, and have severely impaired vision from infancy (27). This congenital phenotype in children carrying mutant ATF6α alleles implicates a requisite role for ATF6 during human embryogenesis, most prominently in the development of tissues and cell types of the eye. However, the function of ATF6 in the differentiation of distinct lineages, tissues and organs, or mature cell types from human progenitor cells, stem cells, or the single-cell zygote is unknown.

Human embryonic stem cells (hESCs) and induced pluripotent stem cells (iPSCs) can undergo differentiation into primary germ layer lineages that ultimately generate distinct cell types and tissues in vitro (32–35). Here, we took advantage of the unique ability of stem cells to recapitulate many features of embryogenesis to elucidate the function of ATF6 during human stem cell differentiation. We used a newly identified small-molecule activator of ATF6 to assess how ATF6 signaling affected stem cell differentiation into early germ cell layers and functional cell types (36). Conversely, we examined how impairment of ATF6 signaling affected early human stem cell differentiation using iPSCs generated from patients that were homozygous for loss-of-function ATF6α alleles (11, 27). Our data revealed that ATF6 signaling positively promoted stem cell differentiation and, unexpectedly, that ATF6 also steered differentiating cells toward a mesodermal cell fate and the robust generation of functional cell types of mesodermal provenance.

RESULTS

The small-molecule AA147 activates ATF6 signaling in human stem cells to influence their differentiation

To study the role of ATF6 in stem cell differentiation, we took advantage of a recently identified small-molecule ER proteostasis regulator *N*-(2-hydroxy-5-methylphenyl)-3-phenylpropanamide (AA147) that selectively activated the ATF6 signaling pathway and a chemically modified analog of AA147, RP22, that did not activate ATF6 signaling, as a control, in our studies (Fig. 1A) (36). We found that the addition of AA147, but not of RP22, to the medium of epithelial cells or stem cells induced ATF6 signaling to similar degrees as treatment with chemical ER stress inducers [dithiothreitol (DTT) or thapsigargin (Tg)], as shown by the increased levels of the cleaved ATF6 cytosolic transcriptional activator fragment [ATF6(N)] (Fig. 1, B and C, and fig. S1). Consistent with AA147-induced ATF6 activation in stem cells, we observed increased amounts of a well-defined transcriptional target of ATF6(N), the ER chaperone GRP78/BiP (Fig. 1C and fig. S1) (9, 10). When we

examined gene expression in these stem cells by RNA sequencing (RNA-seq), we saw an induction of multiple ATF6 transcriptional target genes that regulate ER homeostasis, proteostasis, and ER-associated degradation (ERAD), specifically in stem cells treated with AA147 compared to RP22-treated controls (Fig. 1D and table S1). We confirmed by quantitative reverse transcription polymerase chain reaction (qRT-PCR) that mRNA levels of several ATF6 targets genes (*HERPUD1, EDEM1, GRP78/BiP*, and *SEL1L*) were increased in both AA147-treated stem cells, to similar degrees as seen in our RNA-seq data set, and in other AA147-treated mammalian cell types obtained previously (Fig. 1E) (36). In contrast to the induction of ATF6 target genes seen in our RNA-seq gene expression data set, we found no effect of AA147 on several other signaling pathways in stem cells (fig. S2). Notably, we observed no substantial cell death in stem cells treated with AA147 by visual inspection, by immunoblotting of an apoptosis marker, and by analysis of cell death pathway gene expression in our RNA-seq data set (Fig. 1C and figs. S1 and S2) (37). In contrast, we saw substantial poly[adenosine diphosphate (ADP)–ribose] polymerase (PARP) cleavage and morphologic damage in stem cells treated with Tg (Fig. 1C). Our findings demonstrated that AA147 selectively activated the ATF6 signaling pathway in stem cells with no apparent toxicity after sustained exposure.

Next, we compared our RNA-seq data sets from AA147- and RP22-treated stem cells with published gene expression data sets collected from diverse human cell lines and tissue types (tables S3 and S4). Correlation analysis of RNA-seq profiles revealed that the gene expression signature of our experimental stem cell line (HUES9) was, as expected, similar to those seen in other stem cell and primitive cell types (H7-hESC and H1-hESC; Fig. 1F). Stem cells treated with the inactive control compound RP22 retained a gene expression signature that correlated to other stem and pluripotent cells (Fig. 1F). Unexpectedly, AA147-treated stem cells showed a gene expression signature that was significantly distant from hESCs and primitive cell types and, instead, was grouped with cell types and tissues of predominantly mesendodermal origin (smooth muscle, human skeletal muscle, and myoblasts) (Fig. 1F). Together, the data showed that the small-molecule AA147, in addition to activating ATF6 signaling in stem cells, also unexpectedly altered their course of differentiation.

ATF6 activation suppresses pluripotency and promotes mesodermal differentiation in stem cells

Differentiation of hESCs entails loss of pluripotency, followed by generation of ectodermal, endodermal, and mesodermal germ layers over about the first week of in vitro differentiation (34). To investigate how ATF6 influenced pluripotency and early stem cell differentiation steps, we compared the expression of marker genes specific for these differentiation events in AA147-treated and control samples. In the RNA-seq data set collected from AA147-treated stem cells, we found a significantly reduced expression of virtually all pluripotency genes in the AA147-treated samples compared to RP22-treated cells (Fig. 2A, left, and table S1). Analysis of mRNA levels of the pluripotency gene *SOX2* (sex-determining region Y box 2) by qRT-PCR showed >90% reduction in AA147-treated samples compared to controls (Fig. 2A, right), consistent with the results obtained by RNA-seq.

We next compared expression of ectodermal, endodermal, and mesodermal marker genes in AA147-treated and control stem cell samples. We found selective induction of virtually all mesodermal markers in AA147-treated samples compared to controls by RNA-seq analysis (Fig. 2B, left, and table S1). We confirmed by qRT-PCR the robust induction of the mesodermal marker *ACTA2* (smooth muscle actin–α) in AA147-treated samples (Fig. 2B, right). In contrast, we saw no change in or weak suppression of the amounts of endodermal-specific genes by RNA-seq and qRT-PCR in AA147-treated samples compared to controls (Fig. 2C and table S1). For ectodermal markers, we saw a markedly suppressed expression of many genes by RNA-seq; that of the ectodermal lineage selector *PAX6* (paired homeobox 6) in AA147-treated cells compared to controls was confirmed by qRT-PCR (Fig. 2D and table S1). These data revealed that AA147-induced ATF6 activation in stem cells suppressed pluripotency gene expression and preferentially committed cells to the mesodermal lineage during differentiation. Notably, mesodermal gene induction by AA147 treatment appeared unique to stem cells and was not seen in human embryonic kidney (HEK) 293 cells (fig. S3).

To directly confirm that ATF6 activation in stem cells promoted mesodermal differentiation, we transduced differentiating hESCs with adenovirus (AD) expressing ATF6(N). We analyzed gene expression after 3 days because the viral expression of ATF6(N) beyond this time point was deleterious to hESC viability. We found strong induction of ATF6 transcriptional target genes after viral ATF6(N) transduction compared to hESCs transduced with GFP (Fig. 3A). We also observed uniform increase in mesodermal gene expression after ATF6(N) expression compared to GFP (Fig. 3B).

To determine whether the effects of AA147 on hESC differentiation required ATF6 activation, we treated hESCs with the small-molecule ATF6 inhibitor, Ceapin-A7 (38). Ceapin-A7 inhibits ATF6 signaling by trapping the full-length ATF6 molecule in the ER, thereby preventing the generation of ATF6(N) transcriptional activator (39). We found that Ceapin-A7 administration abolished the ability of AA147 to up-regulate ATF6 target genes in hESCs (Fig. 3C). We also found that concomitant administration of Ceapin-A7 with AA147 prevented the transcriptional induction of mesodermal genes found with AA147 treatment alone (Fig. 3D). These findings demonstrated that AA147's effects on hESCs required ATF6 signaling.

ATF6 impairment promotes pluripotency and impedes mesodermal development

To further investigate the role of ATF6 in early stem cell differentiation, we examined iPSCs generated from patient fibroblasts carrying a missense variant that converts Arg^{324} to a cysteine residue (R324C) in the bZIP domain of ATF6 (Fig. 4, A and B), thereby impairing its transcriptional activity (11, 27). For these experiments, we compared ATF6[R324C] iPSCs generated from patients homozygous for the allele ($ATF6^{R324C/R324C}$) with iPSCs generated from parents that were heterozygous for the allele ($ATF6^{R324C/+}$) (Fig. 4, A and B). We previously demonstrated that heterozygous $ATF6^{R324C/+}$ fibroblasts retained ATF6 signaling activity, whereas ATF6 transcriptional activity was abolished in homozygous $ATF6^{R324C/R324C}$ cells (11, 27). We confirmed that $ATF6^{R324C/R324C}$ iPSCs, like their cognate fibroblasts, were unable to increase the amounts of *GRP78/BiP* mRNA and protein, whereas heterozygous iPSCs retained ATF6 transcriptional activity (Fig. 4, C and D).

Consistent with our previous studies in the patient fibroblasts, full-length ATF6 and cleaved ATF6(N) proteins were present at comparable amounts between heterozygous and homozygous ATF6[R324C] iPSCs (11).

We next asked whether the ATF6-activating small-molecule AA147 could rescue the ATF6 signaling defects found in homozygous $ATF6^{R324C/R324C}$ mutant cell lines (Fig. 4D). In control heterozygous $ATF6^{R324C/+}$ iPSC lines, AA147 increased $GRP78/BiP$ mRNA levels (Fig. 4D), similar to intensities observed with other cell types (Fig. 1). However, no induction of $GRP78/BiP$ was seen when AA147 was applied to homozygous $ATF6^{R324C/R324C}$ iPSC lines (Fig. 4D), although both full-length and cleaved ATF6 proteins were present at comparable amounts between heterozygous and homozygous iPSCs (Fig. 4C). These results showed that AA147 required ATF6 transcriptional activity to exert its pharmacologic effects. These results were consistent with AA147's proposed molecular mechanism of action that involved enhanced trafficking of the full-length ATF6 from ER to Golgi to increase the production of the cleaved ATF6(N) transcriptional activator fragment. However, because the cleaved ATF6(N) fragments in $ATF6^{R324C/R324C}$ cells all contained the R324C mutation, their DNA binding capacity and associated transcriptional activator ability remained compromised irrespective of AA147's promotion of ATF6(N) fragment generation.

Next, we examined the differentiation potential of iPSCs with defective ATF6 activity. When we compared transcriptional levels of pluripotency markers in heterozygous and homozygous ATF6(R324C) iPSCs, we found that $ATF6^{R324C/R324C}$ iPSCs expressed greater amounts of pluripotency genes $POU5F1$ and $NANOG$ than did $ATF6^{R324C/+}$ cells (Fig. 4E). When we examined the levels of ectodermal, endodermal, and mesodermal gene markers, we found that $ATF6^{R324C/R324C}$ iPSCs showed reduced expression of mesodermal marker $ACTA2$ and increased expression of ectodermal marker $PAX6$ compared to heterozygous control iPSCs (Fig. 4F). These studies showed that stem cells lacking ATF6 function retained more pluripotency gene expression and showed altered lineage commitment compared to heterozygous controls. In contrast, activation of ATF6 in stem cells suppressed pluripotency and steered stem cells toward a mesodermal fate. Together, our studies of ATF6-activating drug AA147's effects on stem cells, coupled with our analysis of ATF6[R324C] iPSCs, revealed an unexpected role for ATF6 in early human stem cell differentiation, where ATF6 positively promoted stem cell differentiation toward a mesodermal lineage.

ATF6 activation is an essential process for the maturation of the ER during stem cell differentiation

Next, we investigated how ATF6 promotes stem cell differentiation. Numerous ultrastructural studies from the 1950s showed that stem cells, primitive cells, and poorly differentiated cells contained very little of the ER organelle compared to differentiated, specialized, and mature cell types (1, 40–42). The molecular mechanism by which hESCs create more ER as they differentiate is unknown. In studies of immortalized cell lines (Chinese hamster ovary, HeLa, HEK293, and others), ATF6 expanded the ER when cellular biosynthetic and metabolic demands required more of it (43). We hypothesized that ATF6

also drove expansion of ER as part of stem cell differentiation. To examine this, we first measured ER morphology and ATF6 signaling activity in stem cells over the first 3 weeks of differentiation in vitro (Fig. 5).

To assess changes in ER morphology, we performed confocal microscopy analysis of the ER resident protein marker protein disulfide isomerase (PDI). We saw little PDI expression in stem cells analyzed at early stages (Fig. 5A) but observed a more diffuse and reticular expression pattern of PDI expression with progressive differentiation (Fig. 5B), consistent with the growth of the ER. Our immunofluorescence findings were supported by ultrastructural analyses of early and more differentiated stem cells. Very few ER tubules and structures were seen in early age stem cells (Fig. 5C, ×5000, arrowheads), whereas larger, well-tubulated ER was abundantly found in more differentiated hESCs (Fig. 5D). In contrast to the marked expansion of ER seen during differentiation, nuclear size and morphology remained constant at all stages of stem cell differentiation (Fig. 5, A to D). Consistent with results from our imaging studies, immunoblot analyses of protein lysates from stem cells at various stages of differentiation revealed marked increases in the amount of ER resident proteins, including calreticulin (CRT), calnexin (CNX), and the protein transport protein SEC61 (Fig. 5E). When we compared markers of ATF6 signaling in these same samples, we found that ATF6 signaling was also strongly activated during stem cell differentiation, concomitant with ER expansion, as evidenced by the increased generation of cleaved ATF6(N), GRP78/BiP, and unspliced XBP1 (usXBP1) proteins (Fig. 5F). To establish causality between ATF6 activation and ER expansion in stem cells, we transduced the cleaved ATF6(N) transcriptional activator fragment (5) using an adeno-virus ([AD-ATF6(N) or AD-GFP as a control] into hESCs (9). Overexpression of ATF6(N) resulted in increased amounts of ER chaperones and ER protein–folding enzymes including GRP78/BiP and PDI when compared to untransduced or GFP-transduced controls (Fig. 5G) (43–45). Furthermore, ER expansion and ATF6 activation inversely correlated with loss of pluripotency gene expression (Fig. 5H). In summary, these studies revealed a previously unknown physiological function for ATF6 in the growth and development of the ER during early stem cell differentiation.

AA147-treated hESCs differentiate into functional endothelial cells

Our RNA-seq and biochemical studies thus far have demonstrated that ATF6 activation by AA147 promoted stem cell differentiation toward mesodermal lineage, whereas treatment with the inactive AA147 analog RP22 did not alter pluripotency or lineage gene expression. Consistent with spontaneous differentiation into all lineages, after 2 to 3 weeks of differentiation in the presence of RP22, we identified diverse cell types organized as monolayers or three-dimensional organoid structures that are consistent with stem cells undergoing undirected differentiation along all germ cell layer lineages. These included ectodermal derivatives (neuronal rosettes, neuronal cells, and retinal pigment epithelia), mesodermal derivatives (cardiomyocytes and vascular endothelia), and endodermal derivatives (stromal fibroblasts) (Fig. 6A). In contrast, AA147-treated stem cells predominantly produced a monolayer of cells that bore strong (46) morphologic resemblance to monolayers of cultured human umbilical vein endothelial cells (HUVECs) (Fig. 6B), as well as vascular endothelial cells found as scattered populations in stem cell

cultures that underwent undirected spontaneous differentiation (compare Fig. 6B and endothelial cells in Fig. 6A). Consistent with AA147-induced enrichment of vascular endothelial cells, RNA-seq–derived transcriptomes of AA147-treated samples showed pronounced induction of endothelial marker genes compared to RP22-treated controls (Fig. 6C). We further confirmed by qRT-PCR the robust induction of the vascular endothelial-specific genes *PROCR, ITGB1,* and *CD151* in AA147-treated cells compared to RP22-treated cultures (Fig. 6C).

A functional property of vascular endothelial cells is their migration, proliferation, and reorganization into three-dimensional vascular tubules as part of an angiogenic response (47–52). To test whether AA147-treated cells formed vascular tubules, we cultured and passaged cells in endothelial-specific medium that promoted angiogenesis in vitro (Fig. 6D). For comparison, we also cultured RP22-treated cells and HUVECs under the same conditions. After growth and passaging in endothelial medium, we investigated the angiogenic response and quantified the formation of nascent vascular tubules using fluorescence cell tracker (51). HUVECs, as expected, formed many broad tubules consistent with the initiation of angiogenesis in this protocol (Fig. 6E, top left) (51). RP22-derived cells showed little tubulation initiation, and only a small proportion of RP22-derived cells started to migrate toward each other to form short tubules (Fig. 6E, top right). In contrast, many AA147-derived cells migrated and formed tubules under these conditions (Fig. 6E, bottom right). Tubule length was significantly increased in AA147-treated cells compared to RP22-derived cells (Fig. 6F). To evaluate the long-term culture performance of these newly generated endothelial cells, we maintained cells under endothelial-specific culture conditions indefinitely. RP22-treated cultures failed to thrive under these extended culture conditions and were lost after three passages. In contrast, AA147-treated cells thrived under defined endothelial cell culture conditions and progressively matured to undergo in vitro angiogenesis to form longer and larger blood vessel–like tubules (Fig. 6E, lower left). In summary, these studies revealed that AA147 treatment during hESC differentiation not only directed stem cells toward the mesodermal lineage but also ultimately enriched for the production of mature mesodermal cell types such as functional vascular endothelia.

DISCUSSION

The UPR has been extensively studied in the context of cellular pathology: protecting cells from external proteotoxic insults, intracellular protein misfolding mutations, and promoting cell death in the face of insurmountable ER stress. However, the early embryonic or perinatal lethality observed in knockout mice for many key UPR genes and the congenital phenotypes arising in ATF6-hypomorph patients manifest in the absence of external environmental or genetic protein misfolding mutations. These findings suggest that the UPR plays an essential role in vertebrate embryogenesisand early development apart from preserving ER homeostasis in the adult organism. Here, we combined small-molecule activators of the ATF6 pathway coupled with iPSCs developed from patients carrying missense mutations that inhibited ATF6 activity to probe the function of ATF6 during early human stem cell differentiation. We found that ATF6 suppressed pluripotency and promoted human stem cell differentiation, with surprising specificity toward mesodermal lineage fates.

Our study uncovers a novel developmental function for ATF6 in guiding human stem cell differentiation, distinct from ER proteostasis regulation in adult somatic cells.

We propose that a mechanism by which ATF6 promotes stem cell differentiation is by expanding the ER. Our study highlighted the dearth of ER in pluripotent stem cells and the remarkable expansion of ER once stem cells differentiated (Fig. 5). Scant and simplified ER, cytosolic structures, and organelles are common cellular features observed in virtually all primitive, progenitor, and stem cell types when compared to their differentiated counterparts. In multicellular organisms, the process of differentiation requires the production of secreted morphogens, growth factors, and receptors to respond to these signals. The ER is essential for accurate and robust synthesis of secreted and membrane proteins. ER expansion is therefore a requisite step for differentiation to enable stem cells to ramp up the production of intercellular morphogens and receptors. Our data identified ATF6 as the key molecular mediator driving the ER expansion in early differentiating stem cells.

A completely unexpected finding in our studies was that ATF6 signaling not only promoted stem cell differentiation but also robustly guided stem cells and their progeny toward the mesodermal germ layer lineage. Our finding may provide insight into why the notochord, a mesodermally derived organ essential for vertebrate embryogenesis, failed to form in ATF6α/β knockout fish (25). The mechanism by which ATF6 induced mesodermal cell fates is unknown. ATF6 is unlikely to directly transcribe mesoderm marker genes because the overwhelming majority of mesodermal genes induced in our stem cells after ATF6 activation were not transcriptionally regulated by ATF6 in other cell types (fig. S3) (9, 12, 13). A key exception was vascular endothelial growth factor (VEGF). VEGF is a secreted signaling protein that stimulates vasculogenesis and angiogenesis, canonical mesodermal morphogenetic milestones. It was previously shown that ATF6 binds directly to the *VEGF* promoter to up-regulate its transcription (53). Direct transcriptional up-regulation of the *VEGF* gene by ATF6 in stem cells may be a mechanism to specify mesodermal cell fate.

Our current study provides insight into the pathogenesis of retinal diseases arising from loss of ATF6 function. Foveal hypoplasia is a cardinal feature in both achromatopsia and cone-rod dystrophy arising from ATF6 mutations and contributes to the severe vision loss in people with ATF6 mutations. The fovea is a highly specialized neurovascular region found only in mammalian retinas of the primate order. In primates, the fovea comprises an avascular central neural "pit" ringed by a delicate perifoveal capillary bed (54, 55). Foveal development is closely linked to the development of this unique vascular organization (56–58). Our findings demonstrated that ATF6 promoted mesoderm formation and differentiation into mesodermal tissues such as blood vessels. ATF6, acting through its pro-angiogenic function, may be essential to create the precise vascular network in the nascent foveal region of the retina necessary for its development. When ATF6 signaling is lost in people, foveal hypoplasia emerges as a consequence of abnormal retinal vasculature development. Inhibition of ATF6 impaired retinal and choroidal blood growth in experimental mouse models (59).

A striking result of extended ATF6 activation through AA147 administration was the robust generation of functional endothelial cells that could form new blood vessels, as evidenced by

the presence of vascular endothelial gene markers and their morphogenetic assembly into tubules. Previous studies that induce blood vessel differentiation from hESCs or iPSCs have typically involved the addition of VEGF to stem cell differentiation medium (60–65). However, these protocols are inefficient and costly, and vascular endothelia comprise only a small fraction of the differentiated progeny. In contrast, vascular endothelia compromised the vast majority of progeny (>70%) when pluripotent stem cells underwent differentiation in the presence of ATF6 activator without the need for exogenous VEGF administration. Efficient de novo vasculogenesis and angiogenesis could be helpful for common human diseases arising from insufficient blood supply such as myocardiac ischemia, stroke, and brain ischemia (47, 50). Our results create a scientific rationale for new therapeutic strategies to treat these diseases using small-molecule ATF6 activators to restore or promote endothelial cell development and enhance blood vessel growth to tissues and organs.

MATERIAL AND METHODS

Cell culture

hESC line HUES9 was obtained from the Human Embryonic Stem Cell Core Facility at the Sanford Consortium for Regenerative Medicine at the University of California, San Diego (UCSD). hESCs were maintained on a feeder layer of Mitomycin C–treated primary mouse embryonic fibroblasts (MEFs) (EMD Millipore), with daily medium changes of prewarmed conditioned medium supplemented with fibroblast growth factor 2 (FGF2) (6 ng/ml; EMD Millipore). Conditioned medium was prepared by incubating primary MEFs for 24 hours with hESC-specific medium [KnockOut Dulbecco's modified Eagle medium (DMEM) (Life Technologies), 10% KnockOut Serum Replacement (Life Technologies), human Plasmanate (Chapin Healthcare), 1% MEM nonessential amino acids solution (Life Technologies), 1% penicillin/streptomycin (Life Technologies), 1% GlutaMAX (Life Technologies), and 55 μM 2-mercaptoethanol (Thermo Fisher Scientific)]. hESCs were used between passages 36 and 46 for all experiments. hESCs were split every 3 days using accutase (Innovative Cell Technologies Inc.) and spun out at 200g for 5 min (Allegra X-22, Beckman) before replating on freshly prepared primary MEFs. Primary MEFs were plated on to 0.1% gelatin–coated 10-cm dishes using PMEF medium [DMEM (Corning Inc.) and 10% fetal bovine serum (FBS)]. hESCs and newly generated iPSC lines were maintained on Corning Matrigel–coated dishes (Corning Inc.) using the mTESR1 medium (STEMCELL Technologies) at 37°C and 5% CO_2, medium changes were performed daily, and pluripotent cells were passaged every 5 to 7 days using the ReLeSR medium (STEMCELL Technologies). Human fibroblasts were cultured in DMEM containing 10% FBS, with medium changes every 3 days (27).

Human iPSC generation (feeder-dependent)

Primary human fibroblast cells from achromatopsia patients carrying the R324C mutation within the *ATF6* gene (27) were established from skin biopsies (11, 27). iPSCs were generated following the guidelines provided by CytoTune-iPS 2.0 Sendai Reprogramming kit (Life Technologies). Briefly, 2 days before transduction, 75,000 cells per well of human fibroblast cells from each patient (from passage 2) were plated into two individual wells of a six-well dish. Cells were left to recover for 24 hours. One well of each set of wells prepared

for each cell line was used to determine cell quantities before transduction. The reprogramming vectors included the four Yamanaka factors Oct, SOX2, KLF4, and c-MYC, shown to be efficient for reprogramming primary fibroblasts (66, 67). Medium was changed 24 hours after transduction, and the first appearance of cell toxicity was observed 48 hours after virus exposure. Medium was now changed every other day. At day 4, Mito-C–treated primary MEFs feeder cells (EMD Millipore) were prepared using 10-cm culture dishes. Transduced human fibroblasts were counted and plated on MEF feeders at 50,000, 100,000, and 200,000 cells per 10-cm dish. Twenty-four hours after plating, medium was changed to iPSC medium (see above). Around day 12, cell clumps that appeared grew into colonies, which were collected for further culture after 3 to 4 weeks. Individual colonies were collected and expanded starting from 24-well dishes, layered with Mito-C–treated primary MEFs feeder cells (EMD Millipore). Expansion of colonies and individual cell lines was performed. iPSC lines that were used for experimental procedures were utilized from passages 10 to 17. Multiple independent iPSC lines were successfully established from each patient. All iPSC lines expressed pluripotency markers and showed the ability to differentiate into all three germ layers using the embryoid body (EB) formation procedure.

hESC and iPSC differentiation

For spin EB formation of hESC, ESCs were treated with 5 mM Stemolecule (Stemgent) 24 hours before the procedure. Accutase (Innovative Cell Technologies Inc.) was used to detach cells before performing cell counting using a hemocytometer. A total of 10,000 cells were plated into each well of a 96 V-shaped plate (VWR) in the absence of FGF2 using the differentiation medium [KnockOut DMEM (Life Technologies), 20% KnockOut Serum Replacement (Life Technologies), 1% MEM nonessential amino acids solution (Life Technologies), 1% penicillin/streptomycin (Life Technologies), 1% GlutaMAX (Life Technologies), and 55 μM 2-mercaptoethanol (Thermo Fisher Scientific)]. Plates were spun down at 950g for 5 min (Allegra X-22, Beckman) before placing at 37°C and 5% CO_2 to encourage differentiation. Suspension cultures were prepared 24 hours after EB preparation, and EBs were transferred into ultralow attachment six-well microplates (Corning Inc.) for 5 days, at which point EBs were plated onto Corning Matrigel–coated dishes (Corning Inc.) for further differentiation. Throughout differentiation, samples were collected at indicated time points. Differentiation medium containing required drug treatments or compounds was changed daily.

For iPSCs, 24 hours before differentiation, medium was changed to differentiation medium (see above) to prime cells for induction of differentiation. On the day of EB formation pluripotent, human iPSCs (hiPSCs) were treated with dispase (5 mg/ml; STEMCELL Technologies) for 6 min at 37°C and 5% CO_2. A cell scraper was used to carefully detach the cells before hiPSC colonies were broken up into small cell clumps using a 5-ml surgical pipette. Cells were cultured in ultralow attachment six-well microplates (Corning Inc.) for 6 days, at which point EBs were plated onto Corning Matrigel–coated dishes (Corning Inc.) for further differentiation. Differentiation medium containing required drug treatments or compounds was changed daily, and samples were collected at indicated time points.

Transient transfection in HEK293T cells

HEK293T cells were maintained at 37°C and 5% CO_2 in DMEM (Mediatech) supplemented with 10% fetal calf serum (Mediatech) and 1% penicillin/streptomycin (Invitrogen). To express the wild-type ATF6 with FLAG-tag in the cell culture system, full-length FLAG-tag-ATF6(373).pcDNA3.1 plasmid was transiently transfected to HEK293T cells using Lipofectamine 2000 (Invitrogen). Dimethyl sulfoxide (DMSO), RP22, or AA147 was added to the medium 4 hours after transfection for a 24-hour treatment. DTT was added to the medium 30 min before collecting the cells. Cells were lysed in SDS lysis buffer [2% SDS and 62.5 mM tris-HCl (pH 6.8) containing protease inhibitors; Sigma-Aldrich) and phosphatase inhibitor (Thermo Fisher Scientific)]. Protein concentrations of the total cell lysates were determined by bicinchoninic acid (BCA) protein assay (Pierce). Equal amounts of protein were loaded onto 10% or 4 to 15% Mini-PROTEAN TGX pre-cast gels (Bio-Rad) and analyzed by Western blot. The following antibodies and dilutions were used: antibody against FLAG at 1:5000 (Sigma-Aldrich) and antibody against glyceraldehyde-3-phosphate dehydrogenase (GAPDH) at 1:5000 (GeneTex). After overnight incubation with primary antibody, membranes were washed in tris-buffered saline (TBS) with 0.1% Tween 20, followed by incubation of a horse-radish peroxidase (HRP)–coupled secondary antibody (Cell Signaling Technology). Immunoreactivity was detected using the SuperSignal West chemiluminescent substrate (Pierce).

Compound preparation

ATF6-activating compound AA147 and its analog RP22 was prepared in DMSO as stock solution of 10 mM, and working aliquots were prepared and stored at −20°C. The compound was used in differentiation medium at a final concentration of 10 μM. DMSO was used as drug solvent control but was excluded from data presentation when AA147 and RP22 were used because no difference between RP22- and DMSO-treated samples was detected. ATF6-inhibiting compound Ceapin-A7 was prepared in DMSO as stock solution of 12.5 mM, and working aliquots were prepared and stored at −20°C. The compound was used at a final concentration of 9 μM, and DMSO was used as drug solvent control.

qRT-PCR

Cells were lysed, and total RNA was collected (RNeasy Mini kit, Qiagen). mRNA was reverse-transcribed using the iScript cDNA Synthesis kit (Bio-Rad). For quantitative PCR analysis, complementary DNA (cDNA) was used as template in SYBR Green qPCR Supermix (Bio-Rad). *RPL19* mRNA levels, a transcript whose levels are not altered by ER stress, was used as the normalization standard. Primer and PCR conditions were as follows: *POU5F1*, 5′-CTTGCTGCAGAAG-TGGGTGGAGGAA-3′ (forward) and 5′-CTTGCTGCAGAAGTG-GGTGGAGGAA-3′ (reverse); *NANOG*, 5′-TTCTTGCATCTGCT-GGAGGC-3′ (forward) and 5′-AGTGTGGATCCAGCTTGTCCC-3′ (reverse); *SOX2*, 5′-AGTCTCCAAGCGACGAAAAA-3′ (forward) and 5′-GCAAGAAGCCTCTCCTTGAA-3′ (reverse); *PAX6*, 5′-CCAGGGCAATCGGTGGTAGT-3′ (forward) and 5′-ACGGGCAC-TCCCGCTTATAC-3′ (reverse); *ACTA2*, 5′-GGAGTTATGGTGGG-TATGGGTC-3′ (forward) and 5′-

AGTGGTGACAAAGGAGTAGC-CA-3′ (reverse); *FOXA2*, 5′-
CTACGCCAACATGAACTCCA-3′ (forward) and 5′-GAGGTCCATGATCCACTGGT-3′
(reverse); *ATF6*, 5′-TCCAGCAGCACCCAAGACTC-3′ (forward) and 5′-
CCAGCAACAGCAAGGACTG-3′ (reverse); *GRP78/BiP*, 5′-
CGGGCAAAGATGTCAGGAAAG-3′ (forward) and 5′-
TTCTGGACGGGCTTCATAGTAGAC-3′ (reverse); *HERPUD1*, 5′-
AACGGCATGTTTTGCATCTG-3′ (forward) and 5′-GGGGAA-
GAAAGGTTCCGAAG-3′ (reverse); *EDEM1*, 5′-TTCCCTCC-TGGTGGAATTTG-3′
(forward) and 5′-AGGCCACTCTGCTTTC-CAAC-3′ (reverse); *SEL1L*, 5′-
ATCTCCAAAAGGCAGCAAGC-3′ (forward) and 5′-TGGGAGAGCCTTCCTCAGTC-3′
(reverse); *SPARC*, 5′-GAGAAGGTGTGCAGCAATGA-3′ (forward) and 5′-
AGGACGTTCTTGAGCCAGTC-3′ (reverse); *VEGFB*, 5′-CC-
CTTGACTGTGGAGCTCAT-3′ (forward) and 5′-CACTGG-CTGTGTTCTTCCAG-3′
(reverse); *NKX2.5*, 5′-GGTGGAG-CTGGAGAAGACAG-3′ (forward) and 5′-
AGATCTTGACC-TGCGTGGAC-3′ (reverse); *NODAL*, 5′-CTTCCTGAGCCAACAA-
GAGG-3′ (forward) and 5′-AGGTGACCTGGGACAAAGTG-3′ (reverse); *PAR1*, 5′-
TCCGGATATTTGACCAGCTC-3′ (forward) and 5′-AGGGGAGCACAGACACAAAC-3′
(reverse); *CD73*, 5′-CGCAACAATGGCACAATTAC-3′ (forward) and 5′-CAGGTT-
TTCGGGAAAGATCA-3′ (reverse); *PDGFB*, 5′-ACGGAGAGTGT-GAATGACCA-3′
(forward) and 5′-GATGCAGCTCAGCAAA-TTGT-3′ (reverse); *RPL19*, 5′-
ATGTATCACAGCCTGTACCTG-3′ (forward) and 5′-TTCTTGGTCTCTTCCTCCTTG-3′
(reverse).

Transduction of differentiating hESCs with adenovirus AD-ATF6(N) and AD-GFP

For the transduction of hESC AD, AD-ATF6(N) and AD-GFP as control were generated and
used as previously described (9). Differentiating hESCs were infected at day 14 of
differentiation using 7.5×10^8 copies/ml of each virus. The virus was exposed to the cells
for a total of 3 days, with 2.0 ml of fresh medium added at each day of transduction.
Samples were collected at day 17, and cell lysates were prepared and analyzed by Western
blot and quantitative PCR analysis.

Combined treatment of ATF6 activator AA147 and ATF6 inhibitor Ceapin-A7

Pluripotent hESCs were plated 48 to 72 hours before compound exposure to ensure healthy
cultures. On the day of drug treatment, cells were washed twice with $1\times$ phosphate-buffered
saline (PBS), prewarmed mTESR medium was prepared containing 15 μM AA147 or 15 μM
RP22, and some proportion of the medium was supplemented with 9 μM Ceapin-A7 for
combined treatment. DMSO was used as drug solvent control. hESCs underwent drug
treatment for 4 hours, followed by collection in RLT buffer to collect and isolate RNA,
followed by cDNA synthesis and qRT-PCR analysis.

RNA-seq sample preparation and analysis

Samples for RNA-seq analysis were collected at days 1 and 13 treated with 10 μM RP22 or
10 μM AA47. Three independent experiments were performed. Cells were lysed, and total
RNA was collected (RNeasy Mini kit, Qiagen).

To analyze RNA-seq data, single-end, 100–base pair–long reads from RNA-seq experiments were aligned to the GRCh37.p13 human genome reference assembly using SeqMan NGen 11.2.1 or 12.2.0 (DNASTAR Inc.). The assembly data were then imported into ArrayStar 12.2 with QSeq (DNASTAR Inc.) to quantify the gene expression levels. The sequence counts were normalized to reads per kilobase per million (RPKM) after filtering out non-mRNA sequence features. The statistical significance of the difference between the expression levels of a gene under different conditions was assessed using a Student's t test with the Benjamini-Hochberg false discovery rate (FDR) providing the q value. Raw data are presented in table S2. Data are presented as volcano plots, and visualizing $\log_2$ fold changes in mRNA levels collected by RNA-seq are plotted on the x axis. $\log_{10}$ fold FDR values of RNA-seq data are plotted on the y axis.

To assess correlation in the transcriptome, we constructed a database of RNA-seq transcriptomes from 66 tissues and cell lines using data deposited in Gene Expression Omnibus (GEO) data sets or DNAnexus. Individual SRR (GEO) or ERR (DNAnexus) files were downloaded and aligned as described above for our own RNA-seq data. The accession code(s) for the data sets used are listed in table S4. When multiple data sets were available for a given tissue, their RPKM values were averaged. Pairwise correlation coefficients for the transcriptome expression levels were calculated between each tissue/cell type in table S3 (the square roots of the expression levels were used in the calculation of the correlation coefficients; this reduces the leverage of highly expressed genes on the correlations and also eliminates issues due to taking the logarithm of "0" for genes that are not expressed). We created the transcriptome correlation graph by representing each tissue/cell type as a vertex and connecting the vertices for the tissues/cell types that had correlation coefficients of >0.75. This graph was then divided into communities with a spectral-based clustering method (that is, a method that clusters vertices based on the eigenvalues of the adjacency matrix of the graph), as implemented by the "FindGraphCommunities" command in Mathematica 10.4. Figure 1E shows an enlargement of the part of the full network graph that contains the pretreatment control cells at day 1 (hESC line HUES9), the RP22-treated cells, and the AA147-treated cells at day 13 of differentiation. All calculations were performed using Mathematica 10.4.

For data enrichment analysis, specifically to determine genes, signaling pathways and/or various tissue developments that were not affected by AA147 and showed similarities to RP22-treated samples at day 13, a t test on variance between triplicates of RP22 and AA147 (raw values) was performed. Genes showing a statistically significant variance (P 0.05) were further analyzed and filtered on the basis of percent difference. Genes within ±25% RPKM values of the RP22 were used and filtered on the basis of absolute RPKM values, if >1, counted as true and took to enrichment analysis using http://labs.icahn.mssm.edu/maayanlab/ (68, 69). P value–scored enrichment of cell lines and pathways was determined and presented in volcano plots.

Western blotting

Cells were lysed and sonicated in ice-cold lysis buffer [1% NP-40, 50 mM tris-HCl (pH 8), and 150 mM NaCl containing protease inhibitors (Roche)]. Protein concentrations of total

cell lysates were measured by BCA protein assay kit (Pierce). Total protein (10 μg) was separated using 4 to 15% Mini-PROTEAN TGX precast gels (Bio-Rad), followed by Western blot analysis. The following antibodies and dilutions were used for immunoblotting: antibody against ATF6 at 1:1000 (Abcam), antibody against GRP78/BiP at 1:1000 (GeneTex), anti-PDI at 1:1000 (Stressgen Biotechnologies), antibody against XBP1 at 1:2000 (BioLegend), antibody against SEC61 at 1:1000 (GeneTex), antibody against CNX at 1:1000 (Abcam), antibody against CRT at 1:1000 (Cell Signaling Technology), antibody against cleaved PARP at 1:1000 (Cell Signaling Technology), antibody against GAPDH at 1:5000 (Santa Cruz Biotechnologies), antibody against heat shock protein 90 (HSP90) at 1:5000 (GeneTex), and antibody against GFP at 1:5000 (Santa Cruz Biotechnologies). After overnight incubation with primary antibody, membranes were washed in TBS with 0.1% Tween 20 and incubated in an appropriate HRP-coupled secondary antibody diluted in 5% nonfat milk/TBS with 0.1% Tween 20 for 1 hour. Secondary antibodies used included anti-mouse HRP at 1:5000 (Cell Signaling Technology) and anti-rabbit HRP at 1:7000 (Cell Signaling Technology). Immunoreactivity was detected using the enhanced chemiluminescence assay (Pierce).

Immunofluorescence staining and confocal microscopy

Immunofluorescence analysis was performed on early (day 3) and late stage (day 21) differentiated hESCs. For the early stage EB samples, cell spheres were trypsinized for 10 min and plated on BD Matrigel–coated Millicell EZ slides (EMD Millipore) and left to settle down for 8 hours. Late stage samples were plated directly onto BD Matrigel–coated Milli-cell EZ slides as part of the differentiation protocol on day 5 (EMD Millipore) and cultured with daily medium changes up to day 21. Cells were fixed for 20 min in 4% paraformaldehyde prepared in tissue culture grade PBS (pH 7.4) at room temperature. Samples were washed twice in PBS, followed by permeabilization with 0.1% Triton X-100/PBS. Cells were washed twice with 1% bovine serum albumin (BSA)/PBS, blocked with 10% goat or donkey serum (Jackson ImmunoResearch), and diluted in 1% BSA/PBS for 20 min at room temperature depending on the antibody used. Cells were incubated at room temperature for 1 hour with the 1:250 rabbit polyclonal antibody against PDI antibody (Stressgen Biotechnologies). Samples were washed three times with 0.1% BSA/PBS, followed by secondary antibody incubation using wither 1:500 Alexa Fluor 546 goat antibody against rabbit (red) or 1:500 Alexa Fluor 594 goat antibody against mouse (red) (Molecular Probes). Cell samples were washed three times in PBS and mounted in ProLong Gold antifade reagent with 4′,6-diamidino-2-phenylindole (Life Technologies). Images were collected using an Olympus FluoView 1000 confocal microscope and processed using the Olympus FluoView version 2.0a viewer software at the UCSD microscopy facility (https://neurosciences.ucsd.edu/research/microscopy-core/Pages/default.aspx).

Sample preparation for transmission electron microscopy analysis

Early (day 5) and late stage (day 21) differentiating hESCs were generated as described above. Cell samples were prepared for imaging at the UCSD Cellular and Molecular Medicine Transmission Electron Microscopy Facility (http://emcore.ucsd.edu/TEM.html). Attached cell cultures (day 21) and EB suspension–cultured cells (day 5) were fixed using 2% glutaraldehyde in 0.1 M sodium cacodylate buffer (pH 7.4) for 2 min at room

temperature before incubating on ice for 30 to 60 min. Cells were pelleted by gently scraping attached cells from petri dishes into 2% agarose (Sigma-Aldrich). EB suspension cultures were allowed to settle down using gravitational force before transferring them into 2% agarose. Pellets were fixed again using 2% glutaraldehyde [in 0.1 M sodium cacodylate buffer (pH 7.4)] for at least 4 hours, postfixed in 1% osmium tetroxide in 0.1 M cacodylate buffer for 1 hour, and stained en bloc in 2% uranyl acetate for 1 hour. Samples were dehydrated in ethanol, embedded in Durcupan epoxy resin (Sigma-Aldrich), sectioned at 55 nm on a Leica Ultracut UCT ultramicrotome, and picked up on copper 300-mesh grids. Sections were stained with 2% uranyl acetate for 5 min and with Sato's lead stain for 1 min. Grids were viewed using a JEOL 1200EX II (JEOL) transmission electron microscope and photographed using a Gatan digital camera (Gatan).

Endothelial tube formation assay

HUVECs and AA147- and RP22-derived cells were grown up to reach 90% confluence when they were starved for 24 hours in M200 medium with low serum growth supplement (Thermo Fisher Scientific). Twenty-four–well tissue culture plates were coated with 100 μl of Geltrex LDEV-free reduced growth factor basement membrane matrix (Thermo Fisher Scientific) for 30 min at 37°C. Cells were released and seeded at 4.0×10^5 cells per well. Attached cells were labeled with CellTracker Green CMFDA dye, as per the manufacturer's instructions (Thermo Fisher Scientific). Each well was imaged 8 to 16 hours after seeding at ×4 magnification using an Olympus FluoView 1000 confocal microscope and the National Institutes of Health (NIH) ImageJ version 1.47v software. Tube length was assessed using the ImageJ software (NIH).

Statistical analysis

All results are presented as means ± SD from at least three independent experiments. Student two-tailed t tests (for paired samples) were performed to determine P values. A value of $P < 0.05$ was considered significant. $**P < 0.05$ and $***P < 0.005$.

Supplementary Material

Refer to Web version on PubMed Central for supplementary material.

Acknowledgments

REFERENCES AND NOTES

1. Alberts, B. Molecular Biology of the Cell. 5. Garland Science; New York: 2008.
2. Hiramatsu N, Chiang WC, Kurt TD, Sigurdson CJ, Lin JH. Multiple mechanisms of unfolded protein response–induced cell death. Am J Pathol. 2015; 185:1800–1808. [PubMed: 25956028]

3. Walter P, Ron D. The unfolded protein response: From stress pathway to homeostatic regulation. Science. 2011; 334:1081–1086. [PubMed: 22116877]

4. Nadanaka S, Okada T, Yoshida H, Mori K. Role of disulfide bridges formed in the luminal domain of ATF6 in sensing endoplasmic reticulum stress. Mol Cell Biol. 2007; 27:1027–1043. [PubMed: 17101776]

5. Haze K, Yoshida H, Yanagi H, Yura T, Mori K. Mammalian transcription factor ATF6 is synthesized as a transmembrane protein and activated by proteolysis in response to endoplasmic reticulum stress. Mol Biol Cell. 1999; 10:3787–3799. [PubMed: 10564271]

6. Chen X, Shen J, Prywes R. The luminal domain of ATF6 senses endoplasmic reticulum (ER) stress and causes translocation of ATF6 from the ER to the Golgi. J Biol Chem. 2002; 277:13045–13052. [PubMed: 11821395]

7. Ye Y, Shibata Y, Yun C, Ron D, Rapoport TA. A membrane protein complex mediates retro-translocation from the ER lumen into the cytosol. Nature. 2004; 429:841–847. [PubMed: 15215856]

8. Schindler AJ, Schekman R. In vitro reconstitution of ER-stress induced ATF6 transport in COPII vesicles. Proc Natl Acad Sci USA. 2009; 106:17775–17780. [PubMed: 19822759]

9. Shoulders MD, Ryno LM, Genereux JC, Moresco JJ, Tu PG, Wu C, Yates JR III, Su AI, Kelly JW, Wiseman RL. Stress-independent activation of XBP1s and/or ATF6 reveals three functionally diverse ER proteostasis environments. Cell Rep. 2013; 3:1279–1292. [PubMed: 23583182]

10. Yoshida H, Matsui T, Yamamoto A, Okada T, Mori K. XBP1 mRNA is induced by ATF6 and spliced by IRE1 in response to ER stress to produce a highly active transcription factor. Cell. 2001; 107:881–891. [PubMed: 11779464]

11. Chiang WC, Chan P, Wissinger B, Vincent A, Skorczyk-Werner A, Krawczy ski MR, Kaufman RJ, Tsang SH, Héon E, Kohl S, Lin JH. Achromatopsia mutations target sequential steps of ATF6 activation. Proc Natl Acad Sci USA. 2017; 114:400–405. [PubMed: 28028229]

12. Wu J, Rutkowski DT, Dubois M, Swathirajan J, Saunders T, Wang J, Song B, Yau GDY, Kaufman RJ. ATF6α optimizes long-term endoplasmic reticulum function to protect cells from chronic stress. Dev Cell. 2007; 13:351–364. [PubMed: 17765679]

13. Yamamoto K, Sato T, Matsui T, Sato M, Okada T, Yoshida H, Harada A, Mori K. Transcriptional induction of mammalian ER quality control proteins is mediated by single or combined action of ATF6α and XBP1. Dev Cell. 2007; 13:365–376. [PubMed: 17765680]

14. Jin JK, Blackwood EA, Azizi KM, Thuerauf DJ, Fahem AG, Hofmann C, Kaufman RJ, Doroudgar S, Glembotski CC. ATF6 decreases myocardial ischemia/reperfusion damage and links ER stress and oxidative stress signaling pathways in the heart. Circ Res. 2017; 120:862–875. [PubMed: 27932512]

15. Yoshikawa A, Kamide T, Hashida K, Ta HM, Inahata Y, Takarada-Iemata M, Hattori T, Mori K, Takahashi R, Matsuyama T, Hayashi Y, Kitao Y, Hori O. Deletion of *Atf6α* impairs astroglial activation and enhances neuronal death following brain ischemia in mice. J Neurochem. 2015; 132:342–353. [PubMed: 25351847]

16. Usui M, Yamaguchi S, Tanji Y, Tominaga R, Ishigaki Y, Fukumoto M, Katagiri H, Mori K, Oka Y, Ishihara H. *Atf6α*-null mice are glucose intolerant due to pancreatic beta-cell failure on a high-fat diet but partially resistant to diet-induced insulin resistance. Metabolism. 2012; 61:1118–1128. [PubMed: 22386934]

17. Hashida K, Kitao Y, Sudo H, Awa Y, Maeda S, Mori K, Takahashi R, Iinuma M, Hori O. ATF6alpha promotes astroglial activation and neuronal survival in a chronic mouse model of Parkinson's disease. PLOS ONE. 2012; 7:e47950. [PubMed: 23112876]

18. Wu J, Ruas JL, Estall JL, Rasbach KA, Choi JH, Ye L, Bostrom P, Tyra HM, Crawford RW, Campbell KP, Rutkowski DT, Kaufman RJ, Spiegelman BM. The unfolded protein response mediates adaptation to exercise in skeletal muscle through a PGC-1α/ATF6α complex. Cell Metab. 2011; 13:160–169. [PubMed: 21284983]

19. Egawa N, Yamamoto K, Inoue H, Hikawa R, Nishi K, Mori K, Takahashi R. The endoplasmic reticulum stress sensor, ATF6α protects against neurotoxin-induced dopaminergic neuronal death. J Biol Chem. 2011; 286:7947–7957. [PubMed: 21131360]

20. Yamamoto K, Takahara K, Oyadomari S, Okada T, Sato T, Harada A, Mori K. Induction of liver steatosis and lipid droplet formation in ATF6α-knockout mice burdened with pharmacological endoplasmic reticulum stress. Mol Biol Cell. 2010; 21:2975–2986. [PubMed: 20631254]

21. Wang M, Kaufman RJ. Protein misfolding in the endoplasmic reticulum as a conduit to human disease. Nature. 2016; 529:326–335. [PubMed: 26791723]

22. Jang WG, Kim EJ, Kim DK, Ryoo HM, Lee KB, Kim SH, Choi HS, Koh JT. BMP2 protein regulates osteocalcin expression via Runx2-mediated *Atf6* gene transcription. J Biol Chem. 2012; 287:905–915. [PubMed: 22102412]

23. Nakanishi K, Sudo T, Morishima N. Endoplasmic reticulum stress signaling transmitted by ATF6 mediates apoptosis during muscle development. J Cell Biol. 2005; 169:555–560. [PubMed: 15897261]

24. Ishikawa T, Taniguchi Y, Okada T, Takeda S, Mori K. Vertebrate unfolded protein response: Mammalian signaling pathways are conserved in Medaka fish. Cell Struct Funct. 2011; 36:247–259. [PubMed: 22067999]

25. Ishikawa T, Okada T, Ishikawa-Fujiwara T, Todo T, Kamei Y, Shigenobu S, Tanaka M, Saito TL, Yoshimura J, Morishita S, Toyoda A, Sakaki Y, Taniguchi Y, Takeda S, Mori K. ATF6α/β-mediated adjustment of ER chaperone levels is essential for development of the notochord in medaka fish. Mol Biol Cell. 2013; 24:1387–1395. [PubMed: 23447699]

26. Ansar M, Santos-Cortez RL, Saqib MA, Zulfiqar F, Lee K, Ashraf NM, Ullah E, Wang X, Sajid S, Khan FS, Aminud-Din M, Smith JD, Shendure J, Bamshad MJ, Nickerson DA, Hameed A, Riazuddin S, Ahmed ZM, Ahmad W, Leal SM. University of Washington Center for Mendelian Genomics. Mutation of *ATF6* causes autosomal recessive achromatopsia. Hum Genet. 2015; 134:941–950. [PubMed: 26063662]

27. Kohl S, Zobor D, Chiang W-C, Weisschuh N, Staller J, Gonzalez Menendez I, Chang S, Beck SC, Garcia Garrido M, Sothilingam V, Seeliger MW, Stanzial F, Benedicenti F, Inzana F, Heon E, Vincent A, Beis J, Strom TM, Rudolph G, Roosing S, Hollander AI, Cremers FPM, Lopez I, Ren H, Moore AT, Webster AR, Michaelides M, Koenekoop RK, Zrenner E, Kaufman RJ, Tsang SH, Wissinger B, Lin JH. Mutations in the unfolded protein response regulator *ATF6* cause the cone dysfunction disorder achromatopsia. Nat Genet. 2015; 47:757–765. [PubMed: 26029869]

28. Xu M, Gelowani V, Eblimit A, Wang F, Young MP, Sawyer BL, Zhao L, Jenkins G, Creel DJ, Wang K, Ge Z, Wang H, Li Y, Hartnett ME, Chen R. *ATF6* is mutated in early onset photoreceptor degeneration with macular involvement. Invest Ophthalmol Vis Sci. 2015; 56:3889–3895. [PubMed: 26070061]

29. Skorczyk-Werner A, Chiang WC, Wawrocka A, Wicher K, Jarmu -Szymczak M, Kostrzewska-Poczekaj M, Jamsheer A, Ploski R, Rydzanicz M, Pojda-Wilczek D, Weisschuh N, Wissinger B, Kohl S, Lin JH, Krawczynski MR. Autosomal recessive cone-rod dystrophy can be caused by mutations in the *ATF6* gene. Eur J Hum Genet. 2017; 25:1210–1216. [PubMed: 28812650]

30. Kohl, S., Jagle, H., Wissinger, B. GeneReviews®. Pagon, RA.Adam, MP.Ardinger, HH.Wallace, SE.Amemiya, A.Bean, LJH.Bird, TD.Fong, CT.Mefford, HC.Smith, RJH., Stephens, K., editors. University of Washington; 1993.

31. Remmer MH, Rastogi N, Ranka MP, Ceisler EJ. Achromatopsia: A review. Curr Opin Ophthalmol. 2015; 26:333–340. [PubMed: 26196097]

32. Kopper O, Benvenisty N. Stepwise differentiation of human embryonic stem cells into early endoderm derivatives and their molecular characterization. Stem Cell Res. 2012; 8:335–345. [PubMed: 22286009]

33. Murry CE, Keller G. Differentiation of embryonic stem cells to clinically relevant populations: Lessons from embryonic development. Cell. 2008; 132:661–680. [PubMed: 18295582]

34. Thomson JA, Itskovitz-Eldor J, Shapiro SS, Waknitz MA, Swiergiel JJ, Marshall VS, Jones JM. Embryonic stem cell lines derived from human blastocysts. Science. 1998; 282:1145–1147. [PubMed: 9804556]

35. Takahashi K, Okita K, Nakagawa M, Yamanaka S. Induction of pluripotent stem cells from fibroblast cultures. Nat Protoc. 2007; 2:3081–3089. [PubMed: 18079707]

36. Plate L, Cooley CB, Chen JJ, Paxman RJ, Gallagher CM, Madoux F, Genereux JC, Dobbs W, Garza D, Spicer TP, Scampavia L, Brown SJ, Rosen H, Powers ET, Walter P, Hodder P, Wiseman

RL, Kelly JW. Small molecule proteostasis regulators that reprogram the ER to reduce extracellular protein aggregation. eLife. 2016; 5:e15550. [PubMed: 27435961]

37. Le Rhun Y, Kirkland JB, Shah GM. Cellular responses to DNA damage in the absence of Poly(ADP-ribose) polymerase. Biochem Biophys Res Commun. 1998; 245:1–10. [PubMed: 9535773]

38. Gallagher CM, Garri C, Cain EL, Ang KK-H, Wilson CG, Chen S, Hearn BR, Jaishankar P, Aranda-Diaz A, Arkin MR, Renslo AR, Walter P. Ceapins are a new class of unfolded protein response inhibitors, selectively targeting the ATF6α branch. eLife. 2016; 5:e11878. [PubMed: 27435960]

39. Gallagher CM, Walter P. Ceapins inhibit ATF6α signaling by selectively preventing transport of ATF6α to the Golgi apparatus during ER stress. eLife. 2016; 5:e11880. [PubMed: 27435962]

40. Palade GE, Porter KR. Studies on the endoplasmic reticulum. Studies on the endoplasmic reticulum. I. Its identification in cells in situ. J Exp Med. 1954; 100:641–656. [PubMed: 13211920]

41. Palade GE. Studies on the endoplasmic reticulum. II. Simple dispositions in cells in situ. J Biophys Biochem Cytol. 1955; 1:567–582. [PubMed: 13278367]

42. Palade GE. The endoplasmic reticulum. J Biophys Biochem Cytol. 1956; 2:85–98. [PubMed: 13357527]

43. Bommiasamy H, Back SH, Fagone P, Lee K, Meshinchi S, Vink E, Sriburi R, Frank M, Jackowski S, Kaufman RJ, Brewer JW. ATF6α induces XBP1-independent expansion of the endoplasmic reticulum. J Cell Sci. 2009; 122:1626–1636. [PubMed: 19420237]

44. Thuerauf DJ, Marcinko M, Belmont PJ, Glembotski CC. Effects of the isoform-specific characteristics of ATF6α and ATF6β on endoplasmic reticulum stress response gene expression and cell viability. J Biol Chem. 2007; 282:22865–22878. [PubMed: 17522056]

45. Okada T, Yoshida H, Akazawa R, Negishi M, Mori K. Distinct roles of activating transcription factor 6 (ATF6) and double-stranded RNA-activated protein kinase-like endoplasmic reticulum kinase (PERK) in transcription during the mammalian unfolded protein response. Biochem J. 2002; 366:585–594. [PubMed: 12014989]

46. Recoverin. Lancet. 1991; 337:1257–1258. [PubMed: 1674067]

47. Ausprunk DH, Folkman J. Migration and proliferation of endothelial cells in preformed and newly formed blood vessels during tumor angiogenesis. Microvasc Res. 1977; 14:53–65. [PubMed: 895546]

48. Carmeliet P. Angiogenesis in life, disease and medicine. Nature. 2005; 438:932–936. [PubMed: 16355210]

49. Carmeliet P, Jain RK. Molecular mechanisms and clinical applications of angiogenesis. Nature. 2011; 473:298–307. [PubMed: 21593862]

50. Chung AS, Lee J, Ferrara N. Targeting the tumour vasculature: Insights from physiological angiogenesis. Nat Rev Cancer. 2010; 10:505–514. [PubMed: 20574450]

51. DeCicco-Skinner KL, Henry GH, Cataisson C, Tabib T, Gwilliam JC, Watson NJ, Bullwinkle EM, Falkenburg L, O'Neill RC, Morin A, Wiest JS. Endothelial cell tube formation assay for the in vitro study of angiogenesis. J Vis Exp. 2014:e51312. [PubMed: 25225985]

52. Potente M, Gerhardt H, Carmeliet P. Basic and therapeutic aspects of angiogenesis. Cell. 2011; 146:873–887. [PubMed: 21925313]

53. Ghosh R, Lipson KL, Sargent KE, Mercurio AM, Hunt JS, Ron D, Urano F. Transcriptional regulation of VEGF-A by the unfolded protein response pathway. PLOS ONE. 2010; 5:e9575. [PubMed: 20221394]

54. Sandercoe TM, Geller SF, Hendrickson AE, Stone J, Provis JM. VEGF expression by ganglion cells in central retina before formation of the foveal depression in monkey retina: Evidence of developmental hypoxia. J Comp Neurol. 2003; 462:42–54. [PubMed: 12761823]

55. Provis JM, Dubis AM, Maddess T, Carroll J. Adaptation of the central retina for high acuity vision: Cones, the fovea and the avascular zone. Prog Retin Eye Res. 2013; 35:63–81. [PubMed: 23500068]

56. Provis JM. Development of the primate retinal vasculature. Prog Retin Eye Res. 2001; 20:799–821. [PubMed: 11587918]

57. Provis JM, Penfold PL, Cornish EE, Sandercoe TM, Madigan MC. Anatomy and development of the macula: Specialisation and the vulnerability to macular degeneration. Clin Exp Optom. 2005; 88:269–281. [PubMed: 16255686]

58. Dubis AM, Costakos DM, Subramaniam CD, Godara P, Wirostko WJ, Carroll J, Provis JM. Evaluation of normal human foveal development using optical coherence tomography and histologic examination. Arch Ophthalmol. 2012; 130:1291–1300. [PubMed: 23044942]

59. Liu L, Qi X, Chen Z, Shaw L, Cai J, Smith LH, Grant MB, Boulton ME. Targeting the IRE1α/ XBP1 and ATF6 arms of the unfolded protein response enhances VEGF blockade to prevent retinal and choroidal neovascularization. Am J Pathol. 2013; 182:1412–1424. [PubMed: 23395094]

60. Kane NM, Meloni M, Spencer HL, Craig MA, Strehl R, Milligan G, Houslay MD, Mountford JC, Emanueli C, Baker AH. Derivation of endothelial cells from human embryonic stem cells by directed differentiation: Analysis of microRNA and angiogenesis in vitro and in vivo. Arterioscler Thromb Vasc Biol. 2010; 30:1389–1397. [PubMed: 20431067]

61. Lagarkova MA, Volchkov PY, Philonenko ES, Kiselev SL. Efficient differentiation of hESCs into endothelial cells in vitro is secured by epigenetic changes. Cell Cycle. 2008; 7:2929–2935. [PubMed: 18814342]

62. Nourse MB, Halpin DE, Scatena M, Mortisen DJ, Tulloch NL, Hauch KD, Torok-Storb B, Ratner BD, Pabon L, Murry CE. VEGF induces differentiation of functional endothelium from human embryonic stem cells: Implications for tissue engineering. Arterioscler Thromb Vasc Biol. 2010; 30:80–89. [PubMed: 19875721]

63. Rufaihah AJ, Huang NF, Kim J, Herold J, Volz KS, Park TS, Lee JC, Zambidis ET, Reijo-Pera R, Cooke JP. Human induced pluripotent stem cell-derived endothelial cells exhibit functional heterogeneity. Am J Transl Res. 2013; 5:21–35. [PubMed: 23390563]

64. Song W, Kaufman DS, Shen W. Efficient generation of endothelial cells from human pluripotent stem cells and characterization of their functional properties. J Biomed Mater Res A. 2015; 104:678–687. [PubMed: 26519950]

65. Sriram G, Tan JY, Islam I, Rufaihah AJ, Cao T. Efficient differentiation of human embryonic stem cells to arterial and venous endothelial cells under feeder- and serum-free conditions. Stem Cell Res Ther. 2015; 6:261. [PubMed: 26718617]

66. Takahashi K, Tanabe K, Ohnuki M, Narita M, Ichisaka T, Tomoda K, Yamanaka S. Induction of pluripotent stem cells from adult human fibroblasts by defined factors. Cell. 2007; 131:861–872. [PubMed: 18035408]

67. Takahashi K, Yamanaka S. Induction of pluripotent stem cells from mouse embryonic and adult fibroblast cultures by defined factors. Cell. 2006; 126:663–676. [PubMed: 16904174]

68. Chen EY, Tan CM, Kou Y, Duan Q, Wang Z, Meirelles GV, Clark NR, Ma'ayan A. Enrichr: Interactive and collaborative HTML5 gene list enrichment analysis tool. BMC Bioinformatics. 2013; 14:128. [PubMed: 23586463]

69. Kuleshov MV, Jones MR, Rouillard AD, Fernandez NF, Duan Q, Wang Z, Koplev S, Jenkins SL, Jagodnik KM, Lachmann A, McDermott MG, Monteiro CD, Gundersen GW, Ma'ayan A. Enrichr: A comprehensive gene set enrichment analysis web server 2016 update. Nucleic Acids Res. 2016; 44:W90–W97. [PubMed: 27141961]
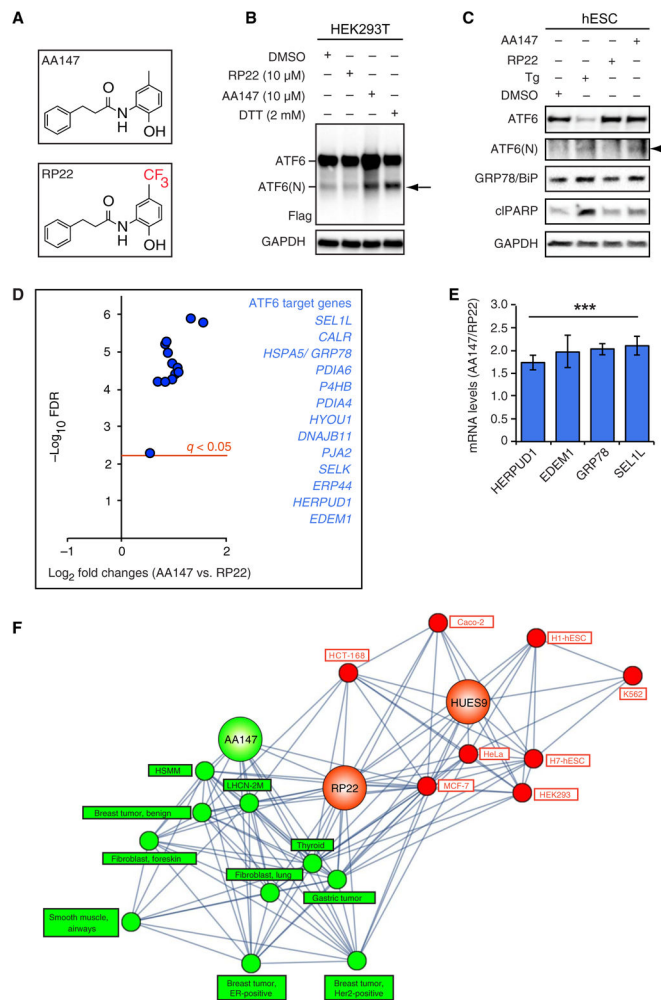
Fig. 1. Small-molecule AA147 activates ATF6 and influences differentiation of stem cells
(**A**) Chemical structures of ATF6 activator AA147 and inactive analog RP22. (**B**) Human embryonic kidney (HEK) 293T cells were transfected with FLAG-tagged ATF6 and cultured with dimethyl sulf-oxide (DMSO), RP22, and AA147 (10 μM) for 24 hours or dithiothreitol (DTT) (2 mM) for 30 min, and lysates were immunoblotted for FLAG-tagged ATF6. Arrow identifies cleaved FLAG-tagged ATF6(N). (**C**) Stem cells were cultured with AA147 and RP22 (15 μM), DMSO, or thapsigargin (Tg; 500 nM) for 4 hours, and lysates were immunoblotted for endogenous ATF6, GRP78/BiP, or cleaved poly[adenosine diphosphate (ADP)–ribose] polymerase (clPARP). Arrow indicates position of ATF6(N). DMSO, drug solvent control; Tg, positive controlforATF6activation; GAPDH (glyceraldehyde-3-phosphate dehydrogenase), loading control. (**D**) Volcano plot representation of RNA sequencing (RNA-seq) data of AA147-treated human embryonic stem cells (hESCs) relative to RP22-treated hESCs at day 13 of differentiation. Blue circles represent ATF6 transcriptional target genes that regulate endoplasmicreticulumassociateddegradation (ERAD), endoplasmic reticulum (ER) homeostasis, and proteostasis (36). FDR, false discovery rate. (**E**) mRNA levels of select ATF6 transcriptional targets, *HERPUD1*, *EDEM1*, *GRP78/BiP*, and *SEL1L*, measured by quantitative reverse transcription

polymerase chain reaction (qRT-PCR). Data are means ± SD from $n = 3$ experiments; ***P < 0.005, Student's two-tailed *t* test. (**F**) Tissue correlation analysis of RNA-seq expression profile of AA147- and RP22-treated hESCs compared with RNA-seq profiles of stem cell line HUES9 and various human cell lines of stem (red) and mesoendodermal (green) origins.
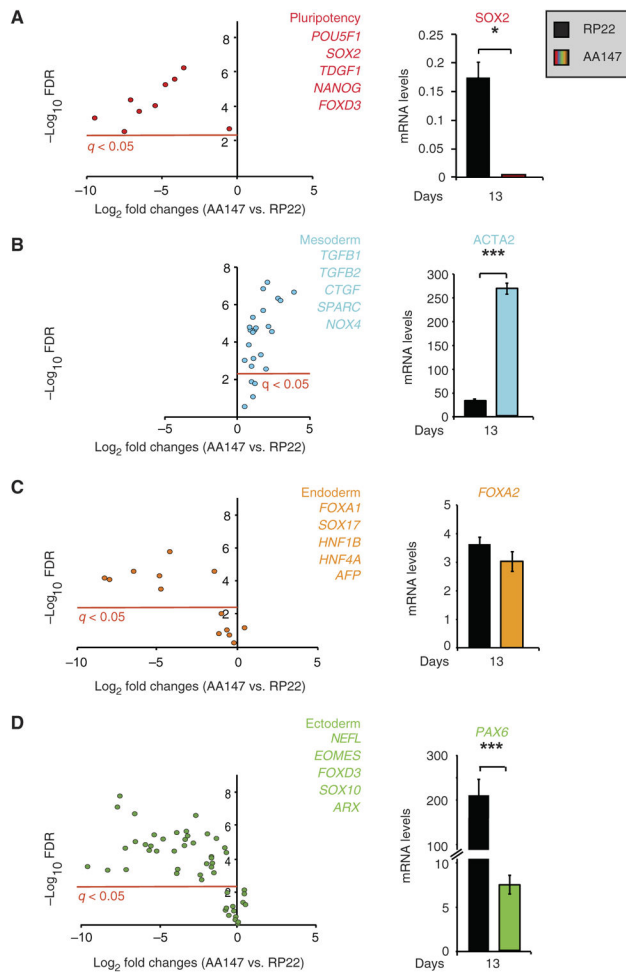
Fig. 2. ATF6 activation by AA147 suppresses pluripotency and induces mesodermal gene expression in stem cells

(**A** to **D**) hESCs were differentiated for 13 days in the presence of 10 μM AA147 or 10 μM RP22. RNA samples were collected for RNA-seq or quantitative PCR analysis. In all cases, AA147- and RP22-treated samples were quantified relative to day 1, and AA147 levels are shown normalized to RP22 at day 13 thereafter. Volcano plots (left) and select qRT-PCR measurements (right) are shown for pluripotency genes (A), mesodermal lineage genes (B), endodermal lineage genes (C), and ectodermal lineage genes (D). The top five most changed genes in each plot are listed. Data are means ± SD for $n = 3$ experiments; $*P < 0.05$ and $***P < 0.005$, Student's two-tailed t test.
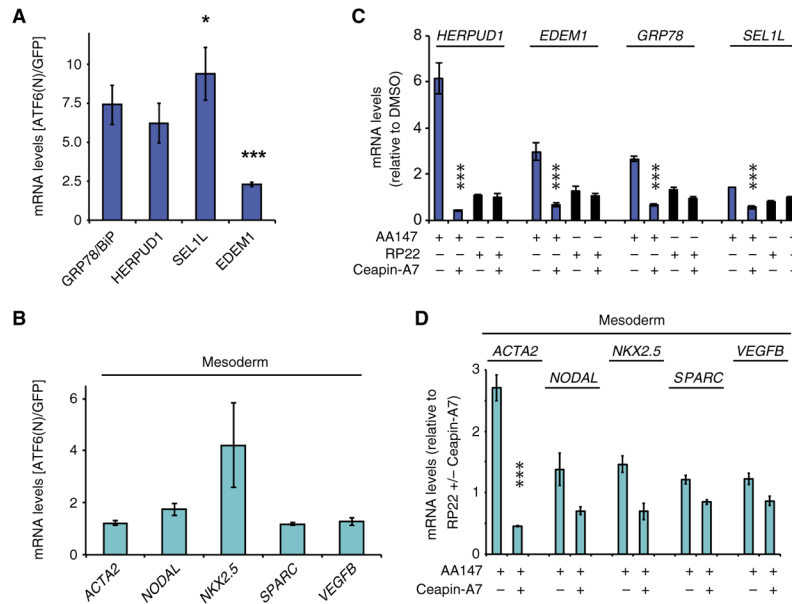
Fig. 3. ATF6(N) induces and Ceapin-A7 opposes mesodermal gene expression in stem cells
(**A** and **B**) qRT-PCR analysis of the expression of ATF6 transcriptional target gene mRNAs
(A) or mesodermal marker mRNAs (B) in hESCs expressing ATF6(N) relative to control
[green fluorescent protein (GFP)–transduced] cells. Lysates were collected 72 hours after
vector transduction. (**C** and **D**) qRT-PCR analysis of the expression of ATF6 transcriptional
target gene mRNAs (C) or mesodermal marker mRNAs (D) in hESCs treated with AA147
(15 μM), RP22 (15 μM), or Ceapin-A7 (9 μM) relative to controls [those treated with DMSO
(C) or RP22 ± Ceapin-A7 (D)]. Lysates were collected ~4 hours after treatment. Data in (A),
(C), and (D) are means ± SD for $n = 3$ (A) and $n = 5$ (C and D) experiments. $*P < 0.05$ and
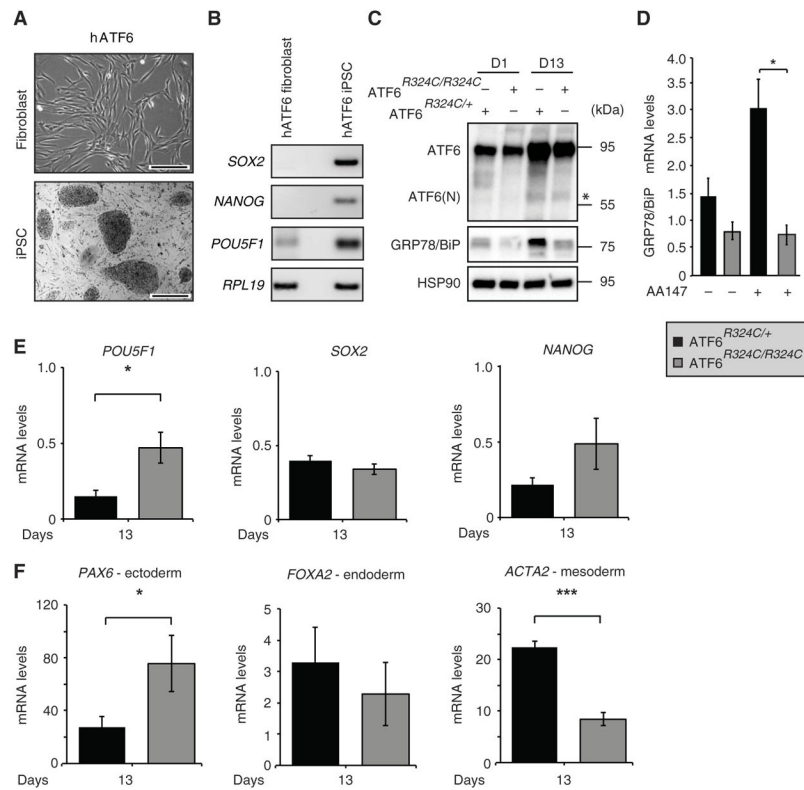$***P < 0.005$, Student's two-tailed t test.

Fig. 4. ATF6-mutant stem cells retain pluripotency and show impaired mesodermal differentiation

(**A**) Representative images of human fibroblasts carrying the ATF6[R324C] mutation and the corresponding iPSC line. Scale bars, 10 μm. (**B**) RT-PCR of pluripotency markers *SOX2*, *NANOG*, and *POU5F1* in a representative human ATF6 fibro-blast line and reprogrammed human ATF6 iPSC line. (**C**) Lysates from heterozygous (*ATF6^{R324C/+}*) and homozygous (*ATF6^{R324C/R324C}*) ATF6 induced pluripotent stem cells (iPSCs) at the indicated days after differentiation were immunoblotted for full-length ATF6, ATF6(N) ("*"), and GRP78/BiP. Heat shock protein 90 (HSP90) functioned as a loading control. D1, day 1; D13, day 13. (**D**) ATF6^{R324C/+} and ATF6^{R324C/R324C} iPSCs were differentiated with AA147 or its analog RP22 for 13 days (10 μM each). *GRP78/BiP* mRNA levels were measured by qRT-PCR. Changes in mRNA expression at day 13 were analyzed relative to day 1 of the respective genotype. (**E**) mRNA levels of pluripotency markers *POU5F1*, *SOX2*, and *NANOG* were measured by qRT-PCR after 13 days of differentiation. (**F**) Expression of an ectodermal lineage marker (*PAX6*), an endodermal lineage marker (*FOXA2*), and a mesodermal lineage marker (*ACTA2*), measured by qRT-PCR after 13 days of differentiation. Amount of mRNA at day 13 was analyzed relative to that at day 1 of the respective genotype. Data in (D) to (F) are means ± SD for $n = 8$ (E and F) and $n = 3$ (D) experiments. *$P < 0.05$ and ***$P < 0.005$, Student's two-tailed *t* test.

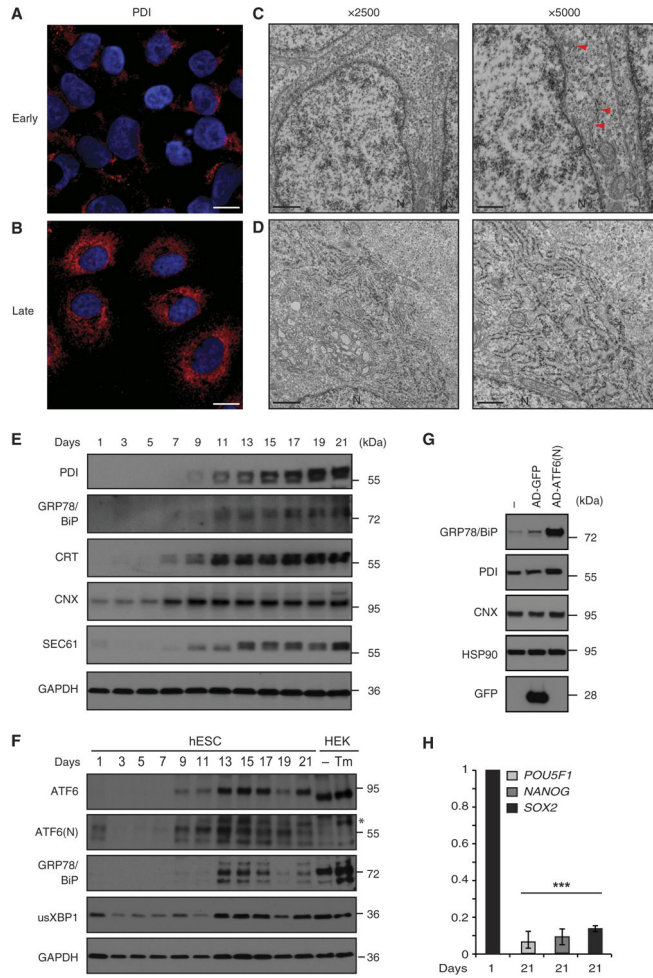**Fig. 5. ATF6 promotes ER expansion as stem cells differentiate**

(**A** and **B**) Confocal immunofluorescence analysis of ER luminal protein, protein disulfide isomerase (PDI) (red), was performed on hESCs at early (A, day 3) and late (B, day 15) stages of differentiation. DAPI (4′,6-diamidino-2-phenylindole) staining (blue) identifies the nuclei. Scale bars, 10 μm. (**C** and **D**) Ultrastructural images were collected from hESCs at early (C, day 3) and late (D, day 15) stages of differentiation. Two magnifications are presented [scale bars, 1 μm (×2500) and 0.5 μm (×5000)]. Arrowheads identify rough ER in early stages of differentiation. N indicates nuclei. (**E**) Immunoblotting for ER proteins PDI, GRP78/BiP, CRT, CNX, and SEC61 in hESC lysates at the indicated day after differentiation. GAPDH blot is a loading control. (**F**) Immunoblotting for ATF6, cleaved ATF6(N) ("*"), GRP78/BiP, and usXBP1 protein abundance in lysates from hESCs at indicated time point after differentiation. Blotting of lysates from HEK293T cells treated with tunicamycin (Tm; 5 μg/ml) was a positive control. GAPDH blot is a loading control. (**G**) Immunoblotting for GRP78/BiP, PDI, and CNX protein abundance in hESCs transduced with adenovirus (AD)–expressing ATF6(N) or GFP. Lysates were collected 72 hours after AD transduction. HSP90 blot is a loading control. (**H**) qRT-PCR analysis of the expression of pluripotency markers *POU5F1*, *NANOG*, and *SOX2* in hESCs at days 1 and 21 of

differentiation. Data in (D) to (F) are means ± SD for $n = 8$ experiments; ***$P < 0.005$, Student's two-tailed t test.
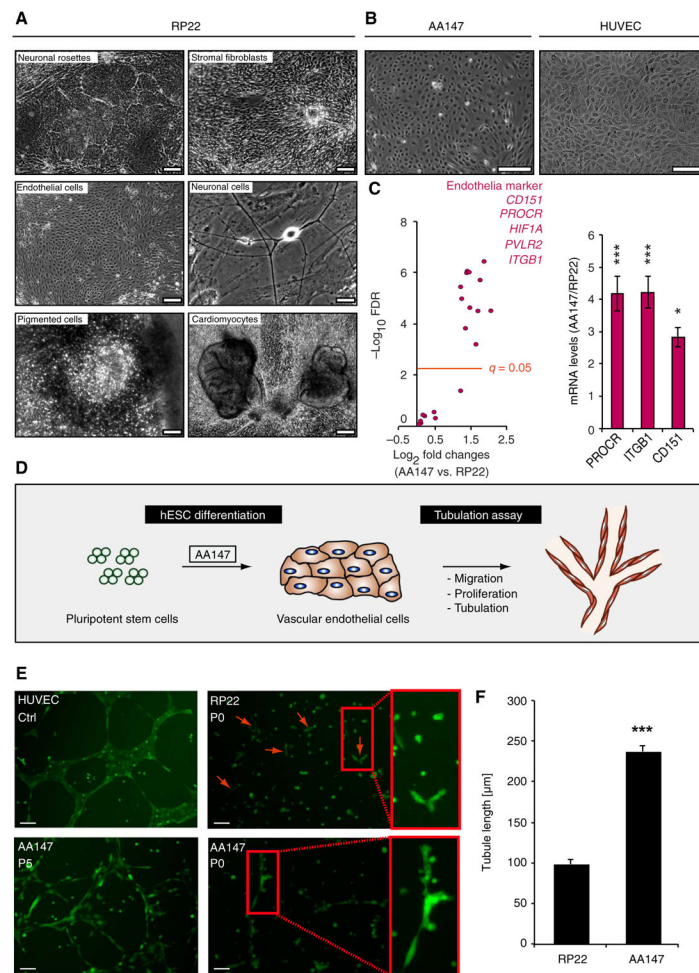
Fig. 6. AA147-treated stem cells preferentially generate vascular endothelial cells
(**A**) Bright-field images of polymorphic hESC cultures after 21 days of undirected differentiation in the presence of RP22 (10 μM). Scale bars, 5 μm. (**B**) A bright-field image shows monomorphic hESC cultures after 13 days of differentiation in the presence of AA147 (10 μM). Scale bars, 10 μm. (**C**) Volcano plot showing endothelia markers in AA147-treated cells relative to RP22-treated cells; the top five most changed genes are listed. Quantitative mRNA levels of endothelial cell markers *PROCR*, *ITGB2*, and *CD151* are shown. Data are shown by quantifying AA147- and RP22-treated samples relative to day 1 and then presenting AA147 relative to RP22 at day 13. (**D**) Schematic representation of differentiation protocol for the generation of endothelial cells for subsequent vascular tubule formation. (**E** and **F**) Cell migration and localization of endothelial cells (labeled with green CellTracker dye) during in vitro vascular tubule formation. Endothelial tubule formations by primary human umbilical vein endothelial cells (HUVECs) are shown as a positive control. Arrows identify endothelial cells undergoing nascent tabulation. (**F**) Length of tubules, quantified by ImageJ, in AA147- and RP22-treated endothelial cells at P0. Data are means ± SD for $n = 4$ (C) and $n = 3$ (F) experiments. *$P < 0.05$ and ***$P < 0.005$, Student's two-tailed t test.